

A Comprehensive Study of Low-Energy Response for Xenon-Based Dark Matter Experiments

L.Wang^a, D.-M. Mei^{a,b,*}

^a*Department of Physics, The University of South Dakota, Vermillion, South Dakota 57069*

^b*School of Physics and Optoelectronic, Yangtze University, Jingzhou 434023, China*

Abstract

We report a comprehensive study of the energy response to low-energy recoils in dual-phase xenon-based dark matter experiments. A recombination model is developed to explain the recombination probability as a function of recoil energy at zero field and non-zero field. The role of e-ion recombination is discussed for both parent recombination and volume recombination. We find that the volume recombination under non-zero field is constrained by a plasma effect, which is caused by a high density of charge carriers along the ionization track forming a plasma-like cloud of charge that shields the interior from the influence of the external electric field. Subsequently, the plasma time that determines the volume recombination probability at non-zero field is demonstrated to be different between electronic recoils and nuclear recoils due to the difference of ionization density between two processes. We show a weak field-dependence of the plasma time for nuclear recoils and a stronger field-dependence of the plasma time for electronic recoils. As a result, the time-dependent recombination is implemented in the determination of charge and light yield with a generic model. Our model agrees well with the available experimental data from xenon-based dark matter experiments.

Key words: Low-energy Recoils, Recombination, Plasma effects.

PACS: 95.35.+d, 07.05.Tp, 25.40.Fq, 29.40.-n

* Corresponding author.

Email address: Dongming.Mei@usd.edu (D.-M. Mei).

1 Introduction

Observations commencing in the 1930s [1] have led to the contemporary and rather shocking view that 96% of the matter and energy in the universe neither emits nor absorbs light or other electromagnetic radiation [2,3]. The most popular candidate for the dark matter is the WIMP (Weakly Interacting Massive Particle), a particle with a mass thought to be comparable to the mass of heavy nuclei, but with feeble and extremely short-range (in the weak-force scale) interaction with atomic nuclei. Theories invoking Supersymmetry (SUSY), being probed currently at the Large Hadron Collider (LHC), naturally provide a particle that could be the WIMP [4]. Most of the mass of the Milky Way galaxy would be WIMPs, and they would interact with matter so rarely that WIMPs would easily pass through the Earth. Very rarely, WIMPs would collide with atomic nuclei, causing the atom to suddenly recoil with a velocity thousands of times that of sound [5]. Many studies over the past decade have emphasized the high priority of WIMP direct detection [6,7]. Over thirty years exploration with many targets, liquid xenon has become a leading technology in the field. The LUX (Large Underground Xenon), XENON100, and PandaX [8,9,10,11] experiments have demonstrated the scalability of xenon detector to multi-ton scale. It is the goal of the successor experiments, LZ (LUX-Zeplin) and XENON1T [12,13] to decisively identify xenon atoms that have suddenly recoiled in response to a collision with a WIMP. Successful identification (known as direct detection) and subsequent studies would transform empirical understanding of cosmology, astrophysics, and particle physics.

The detection of WIMP-induced nuclear recoils (NRs) in a dual-phase xenon detector can be conducted through observation of two anti-correlated and complementary signals: the scintillation photons in liquid and the charge carriers in gas [14,15,16]. It has been shown that the ratio of the charge to light signal can be used to discriminate NRs against electronic recoils (ERs) [8,9,10,11,17]. The energy reconstruction in a dual-phase xenon detector is conducted based on the physics processes involved. An incoming particle with a given kinetic energy, interacts with xenon atoms by depositing energy (E_0) in liquid xenon through many processes, as sketched in Figure 1. The total energy deposited is expended in the production of excitons, e-ion pairs and atomic motion (heat). The Platzman equation [18] is used to describe the conservation of energy:

$$E_0 = N_{ex} \times E_{ex} + N_i \times E_i + N_i \times \varepsilon, \quad (1)$$

where N_i is the number of e-ion pairs produced at the average expenditure of energy E_i , N_{ex} is the number of excitons produced at the average expenditure of energy E_{ex} , and ε is the average kinetic energy of sub-excitation of electrons.

The energy deposition processes create direct excitation and ionization. In a

dual-phase detector, under an electric field, some of the electrons generated through ionization in the liquid are drifted to the gas. Therefore, two signals are measured. The first is the primary scintillation light due to direct excitation and recombination of e-ion pairs in liquid, denoted as $S1$. The second is the proportional scintillation light in gas, denoted as $S2$, which is proportional to the number of electrons escaping the recombination process. One can express

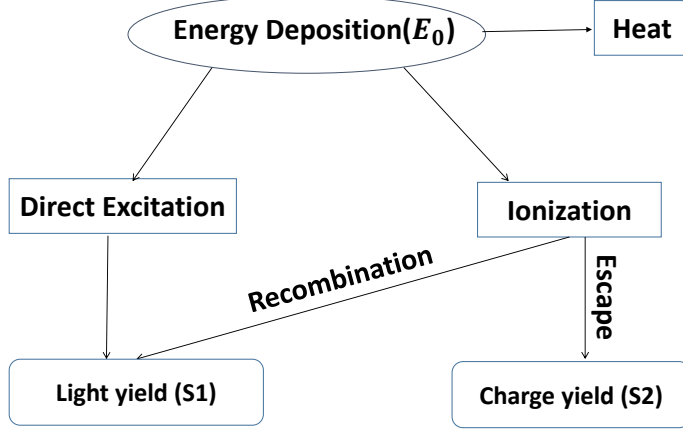


Fig. 1. A schematic energy deposition in dual-phase xenon detectors.

$\langle S1 \rangle = g_1 n_\gamma$ and $\langle S2 \rangle = g_2 n_e$, where n_γ is the number of detected photons in liquid, n_e is the number of electrons detected in the gas phase [19], and g_1 and g_2 are the detector specific gain factors in liquid and gas xenon, respectively.

Since n_e and n_γ are anti-correlated with the recombination probability between electrons and ions in liquid, we can write as a generic model:

$$n_e = N_i(1 - r) = \frac{L \cdot E_0}{W_i}(1 - r), \quad (2)$$

and

$$n_\gamma = N_{ex} + rN_i = \frac{L \cdot E_0}{W_i} \left(r + \frac{N_{ex}}{N_i} \right), \quad (3)$$

where r represents the recombination probability between electrons and ions, L is the quenching factor [20] that has different forms depending on the recoil type, non-zero field and zero field, the W_i -value is the average energy expended per e-ion pair, and $\frac{N_{ex}}{N_i}$ is the exciton-to-ion ratio. The charge yield is defined as $Q_y = \frac{n_e}{E_0}$ while the light yield is defined as $L_y = \frac{n_\gamma}{E_0}$.

To reconstruct the recoil energy, one must know the W_i -value, the quenching

factors, and the recombination probability for a given electric field. The recent measurements from LUX [19], with a D-D neutron generator, together with the available data from other experiments at different fields [21,22,23,24,25], have shown an anti-correlation between the charge and light yield for NRs with the following characteristics: (1) the charge yield increases as recoil energy decreases and (2) the charge yield is weakly dependent on electric field and varies in a relatively narrow band over a large range of electric field from 100 V/cm to 4000 V/cm. The physics mechanisms that are responsible for the observations in the charge yield are not clear in terms of the variation of the W_i -value and recombination. Although the W_i -value is typically treated as a constant, in this work we treat it as energy dependent. However, since its variation is small [26], recombination is, thus, responsible for the observed behaviors. The question becomes what physics mechanisms in the recombination processes cause the observations and why the recombination probability is weakly dependent on the field strength for NRs.

Similarly, the charge yield of ERs with the tritium data from LUX [27] and the data from [28] have shown a distribution that widely spreads over a range from ~ 20 electrons/keV to ~ 50 electrons/keV depending on recoil energy. In addition, the charge yield has a stronger dependence on the applied electric field in comparison with the charge yield of NRs. The question is what causes such a behavior.

In the case of zero field, the observed light yield is usually interpreted as a relative scintillation efficiency with respect to a known gamma-ray energy, such as 122 keV from ^{57}Co calibration source [8,10,17]. The available data from various experiments [29,30,31,32,33,34] shows a rather broad distribution, which deserves a good physics model to justify the observed data points. The observed relative scintillation efficiency can be explained by three physics functions: the variation of the W_i -value, quenching factors, and recombination. We can once again assume that the variation of the W_i -value is small, quenching factors and recombination are responsible for the observed distribution. The question is which one is dominant.

Prior to this work, many authors have modeled ionization, scintillation, and recoil tracks in xenon detectors [23,35,36,37,38,39,40,41,42,43,44,45,46,47]. A global analysis of light and charge yield in liquid xenon offers a data-driven model, which has been popular in the field [48]. In this paper, a comprehensive study of physics mechanisms behind ionization, scintillation, and recoil tracks is discussed. We develop a model in Section 2 to demonstrate the physics mechanisms that govern e-ion recombination for non-zero field and zero field. Subsequently, we implement the model and compare with the available experimental data in Section 3. Section 4 summarizes the significant findings. Section 5 concludes the prediction power and physics implications.

2 Recombination of e-ion pairs

2.1 Recombination model

The light yield is the total effect of direct excitation of xenon atoms and recombination of e-ion pairs created by ionization [49,50]. The recombination probability describes the fraction of electrons that recombine in liquids. Currently, two recombination models are used to calculate the recombination probability: Birks-Doke Law is used for long range ionization tracks (for recoil energy ≥ 10 keV) [51,52]; the Thomas-Imel model is adopted for short range ionization tracks (for recoil energy ≤ 10 keV) [53,54,55].

In this work, we offer an alternative physics model to describe recombination occurring under certain circumstances with respect to different physics processes. For a given energy, the charged particles ionizing atoms along their tracks create e-ion pairs. The ions form rare-gas molecular ions, Xe_2^+ , within picoseconds [56,57,58]. Those molecular ions are localized with an average distance of about 40 nm in liquid xenon for 1 MeV electrons [49]. The primary and secondary electrons are all thermalized along the track. The thermalized electrons recombine with localized Xe_2^+ through formation of the excited molecular states. This suggests that the recombination of e-ion pairs is confined within a specific volume. Within this volume, recombination can be described as two stages with respect to the recombination time scale. The first stage occurs when electrons are thermalized along the ionization track. These thermalized electrons recombine with their own parent ions merely in the ionization zone. This process is called “the parent recombination” [52,55]. In the second stage, the ionization zone is expanded outwards to be a larger zone due to the ambipolar diffusion [59] of electrons and ions. Within this larger zone, thermal electrons recombine with ions other than their own parent ions. This process is named as “the volume recombination” [52,55]. We illustrate a two-zone recombination in Figure 2.

In the ionization zone, thermal electrons are mainly attracted by their own parent ions along the initial ionization track [60,61], and recombine with their own parent molecular ions. The rate of the parent recombination is governed by the parent recombination time, which is independent of electric field. Many previous works employed the Onsager radius in which the parent recombination takes place [62,53,55,63,64,65]. However, the time scale of the parent recombination within the region has not been used in the calculation of the recombination probability. Beyond the ionization zone, the recombination time of e-ion pairs can be very different for non-zero field and zero field. This is because the velocity and the directions of thermal electrons can be greatly affected by the presence of an external electric field.

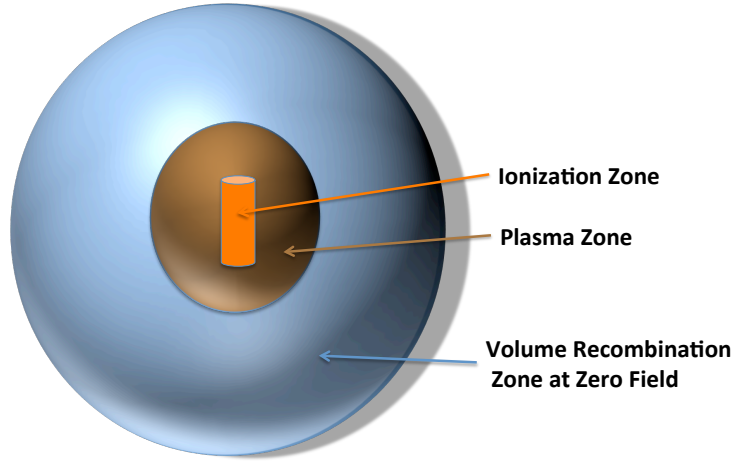


Fig. 2. A schematic for the recombination occurring in the ionization zone, the plasma zone, and the volume recombination zone. The ionization zone is assumed to be a cylinder while both the plasma zone (non-zero field) and the volume recombination zone (zero field) are considered as spherical shape.

The plasma zone is the expansion of the ionization zone in which a high density of charged carriers along the ionization track forms a plasma-like cloud of charge that shields the interior from the influence of the external electric field [50]. Only those charge carriers arriving at the outer edge of the cloud are subject to the influence of the external electric field, and begin to migrate immediately. This plasma-like cloud expands radially due to the ambipolar diffusion of charge carriers and is gradually eroded away until the charges at the interior are finally subject to the external field and also begin to drift. The time needed for the total disintegration of this plasma region is called “the plasma time” and is responsible for the volume recombination at non-zero field. Once the plasma region disappears, the charge carriers are drifted away by the external electric field, and the recombination ceases between electrons and ions [50].

In the absence of an electric field, the ionization zone is expanded due to the ambipolar diffusion process as well. The electrons at the edge of the ionization zone exchange momentum and energy with xenon atoms in the medium, which is controlled by the deformation potential scattering due to the longitudinal acoustic waves [66]. This is because the accompanying acoustic waves generation is required by the momentum conservation in the process of inelastic collisions between electrons and xenon atoms. As the electrons lose energy, the magnitude of acoustic waves generated by the inelastic collision process be-

comes weaker. As a result, the impact of the deformation potential due to the acoustic waves on the electrons becomes smaller, until the velocity of the electrons is equal to the longitudinal sound velocity, 0.65×10^5 cm/s [67] in liquid xenon, and the deformation potential of the acoustic waves disappears, hence the electrons escape recombination. The time that electrons spend to reach the longitudinal sound velocity is called “the volume recombination time” at zero field.

In the above two scenarios regarding non-zero field and zero field, the volume recombination probability is governed by the volume recombination time. At non-zero field, the volume recombination time is equivalent to the plasma time. Combining the parent recombination and the volume recombination together, it is clear that the recombination of e-ion pairs relies on the parent recombination time and the volume recombination time. At time $t = 0$, the recombination probability is 0 and the recombination begins. When t approaches to infinite, the recombination probability approaches to 1 at zero field with a sufficient large detector.

Therefore, the recombination probability, r , representing the probability of recombining in between $t = 0$ and $t = t$, can be postulated as

$$r = 1 - e^{-\lambda t}. \quad (4)$$

The term λ is recombination constant for both the parent recombination and volume recombination. With the assumption that the recombination of e-ion pairs occurs with a probability of 50%, from Eq. 4, $\lambda = \frac{\ln 2}{t_c}$, gives the average recombination time of $t_c = 15$ ns [49]. The final expression of the recombination probability can be expressed by Eq. 5:

$$r = 1 - e^{-\frac{\ln 2}{t_c}(t_{pa} + t_v)}, \quad (5)$$

where t_{pa} is the parent recombination time in the ionization zone and t_v is the volume recombination time. Note that the recombination begins as soon as some electrons are thermalized, with an average thermalization time of 6.5 ns [67], in the ionization zone. The parent recombination continues until all electrons become thermal electrons and the ionization zone expands into the plasma zone, the recombination is thus taken over by the volume recombination. Within the ionization zone, the Onsager radius, electron and its parent ion are very close together, they interact through their Coulomb electric fields as isolated, individual particles. However, as the distance between the electron and its parent ion increases beyond the Onsager radius, they interact simultaneously with many nearby charged particles. This produces a collective interaction as a plasma.

In the plasma zone, the Coulomb force from any given charged particle causes all the nearby charges to move, thereby electrically polarizing the medium. The charge particles are diffused through the ambipolar diffusion process, which is governed by the total number of charge carriers and the strength of external field. Though the plasma time or the volume recombination time depends on the diffusion of charge carriers through multiple scattering, a complicated process - it can be determined as a function of recoil energy using experimental data.

2.2 Volume recombination time for non-zero field

Since the volume recombination time depends on recoil energy under an electric field, if one combines Eq. 2 or Eq. 3 with Eq. 4, it is seen that the volume recombination time can be expressed in the form of a logarithm of recoil energy. To fit the generic model (Eq. 2 or Eq. 3) to data, the volume recombination time, t_v , equivalent to the plasma time, t_{pl} , is parametrized to be energy dependent:

$$t_{pl} = \alpha(\ln E_r) + \beta(\ln E_r)^2, \quad (6)$$

where the quantities α and β are electric field-dependent and recoil type dependent parameters, and can be parametrized by:

$$\alpha = \gamma_1 F^{\delta_1}, \quad (7)$$

and

$$\beta = \gamma_2 F^{\delta_2}, \quad (8)$$

where F is the applied electric field, and γ_1 , γ_2 , δ_1 and δ_2 are free parameters.

As introduced in Section 1, due to the weak field dependence in the charge yield of NRs, we assume α has negligible field dependence, which is determinable with a set of experimental data under a given field. However, β is electric field dependent. In the case of ERs, because of a stronger field dependence in the charge yield of ERs, both α and β are assumed to be field dependent.

At non-zero field, the above parametrization functions are chosen based on the physical arguments that the plasma time depends on the initial ionization density, the diffusion of charge carriers, and the strength of the electric field. The energy-dependent terms arise from the density of the plasma track that confines the diffusion of thermal electrons in Coulomb electric field. When the

plasma zone is formed on the track of the ionizing particle, effective recombination of the thermal electrons with the ions takes place in an ambipolar diffusion process. As the recombination proceeds, the ion density in the zone decreases, until ultimately a time is reached when the positive space charge of the zone cannot retain the electrons. Ideally, two processes can cause diffusion and erosion of the plasma track: (1) the thermal electrons at the edge of plasma zone begin to drift away, under the influence of the external electric field and (2) the recombination within the plasma zone reduces the density of the plasma track. In reality, the plasma zone is a dynamic zone in which diffusion, recombination, and Coulomb attraction alternate on thermal electrons. This dynamic process makes the accurate calculation of the plasma time difficult. However, the plasma time can be determined with reliable experimental data.

Using Eq. 2, Eq. 3, Eq. 5, and Eq. 6, the charge and light yield can be expressed as:

$$Q_y = \frac{L}{W_i} e^{\{-\frac{\ln 2}{t_c}[t_{pa} + \alpha(\ln E_r) + \beta(\ln E_r)^2]\}}, \quad (9)$$

and

$$L_y = \frac{L}{W_i} \left(1 - e^{\{-\frac{\ln 2}{t_c}[t_{pa} + \alpha(\ln E_r) + \beta(\ln E_r)^2]\}} + \frac{N_{ex}}{N_i}\right), \quad (10)$$

2.2.1 Parameters determination for NRs

For NRs, the recently released LUX D-D neutron data [19] show both charge and light yield as a function of nuclear recoil energy. Since the charge and light yield are anti-correlated, one can use the LUX charge yield data to determine the plasma time for NRs. If the model works, it should describe the light yield with an anti-correlation to the charge yield from the LUX data. When using Eq. 9 to fit the LUX D-D neutron data, L is the Lindhard quenching factor described in Eq. 11 [20], W_i is described in Eq. 12 [26,68,69,70], $t_c = 15$ ns, $\frac{N_{ex}}{N_i}$ is described in Eq. 13, E_r is nuclear recoil energy in keV.

$$L = \frac{k \cdot g(\epsilon)}{1 + k \cdot g(\epsilon)}, \quad (11)$$

where $k = 0.133Z^{2/3}A^{-1/2}$, $g(\epsilon) = 3\epsilon^{0.15} + 0.7\epsilon^{0.6} + \epsilon$, and $\epsilon = 11.5E_rZ^{-7/3}$ for a given atomic number, Z , mass number, A , and recoil energy, E_r .

$$W_i = 14.94 + 8.35 \times \frac{N_{ex}}{N_i}. \quad (12)$$

Since $\frac{N_{ex}}{N_i}$ represents the ratio of probability of direct excitation to ionization, it can be parameterized as a function of electron-equivalent recoil energy using the ratio of the cross-section of excitation to ionization:

$$\frac{N_{ex}}{N_i} = \frac{1 - \exp(-I/E_{er})}{3 + \exp(-I/E_{er})}, \quad (13)$$

where I is the mean ionization potential of xenon and E_{er} is electron-equivalent recoil energy. At very low energies, the term with a constant of 3 constrains $\frac{N_{ex}}{N_i}$ to be a maximum value of $\sim 30\%$, in accordance with the acceptable range of 6% to 26% by [26,48,71,62,72,53,49]. The experimental values for I from Barkas and Berger [73,74] can be used to determine $I = 555.57$ eV for xenon.

Figure 3 illustrates the determination of the parameters, t_{pa} , α and β , using the LUX D-D neutron data. As expected, once the values of t_{pa} , α and β are determined using the charge yield from the LUX D-D neutron data, the model also describes the light yield data very well as shown in Figure 3.

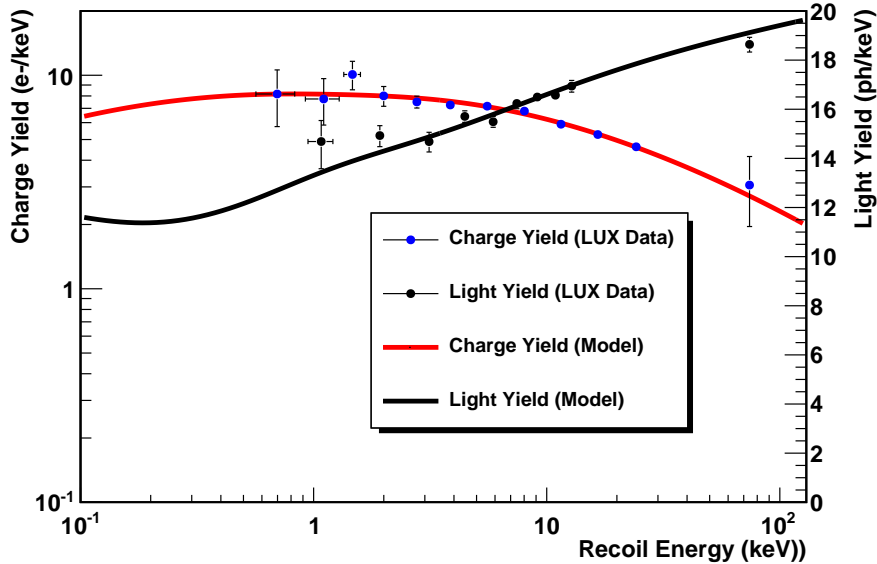


Fig. 3. Determination of t_{pa} , α and β by fitting Eq. 9 and Eq. 10 into the LUX D-D neutron data. $t_{pa} = 1.5 \pm 0.5$ ns, $\alpha = 3.617 \pm 0.521$ ns and $\beta = 1.313 \pm 0.196$ ns at 181 V/cm with $\chi^2/ndf = 4.299/9$. The word “Model” in the legend represents the generic model with the Wang-Mei’s recombination probability from this work.

One can fit the model, Eq. 9, into the data available from experiments with different electric fields to look into the field dependence of t_{pa} , α and β . Before doing so, we notice that t_{pa} is independent of electric field since the external field cannot penetrate the ionization zone. Therefore, we treat t_{pa} as constant. Figure 4 shows a weak dependence on the electric field.

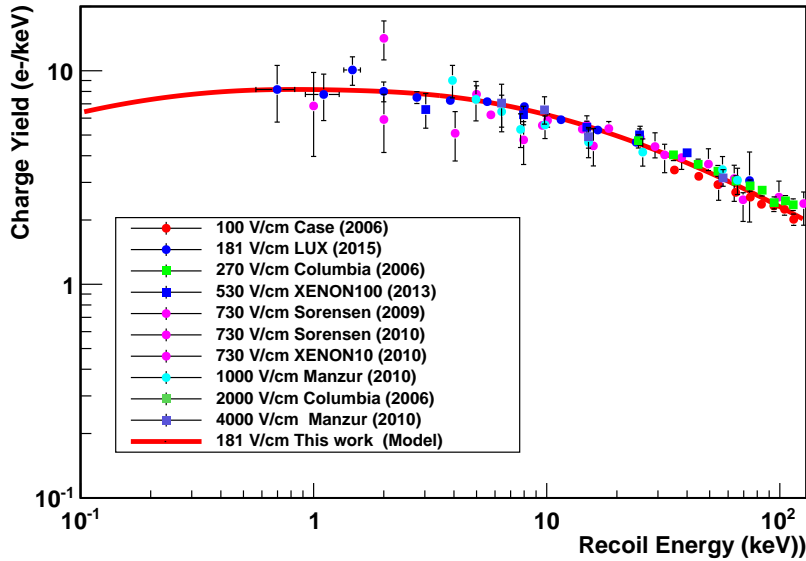


Fig. 4. A charge yield comparison between the generic model in Eq. 9 and data taken with different field strengths using the plasma time determined from the LUX data. The data in this plot are from Case (2006) at 100 V/cm [14], LUX D-D (2015) at 181 V/cm [19], Columbia (2006) at 270 V/cm [14], XENON100 (2013) at 530 V/cm [21], Sorensen (2009) at 730 V/cm [22], Sorensen (2010) at 730 V/cm [23], XENON10 (2010) at 730 V/cm [24], Manzur (2010) at 1000 V/cm [25], Columbia (2006) at 2000V/cm [14], and Manzur (2010) at 4000 V/cm [25]. The word “Model” in the legend represents the generic model with the Wang-Mei’s recombination probability from this work.

Furthermore, we found that α is independent of the field and the value of $\delta_1 = 0$ in Eq. 7 and $\gamma_1 = \alpha$. The values of β is found to be weakly depended on the field and the value of δ_2 in Eq. 8 is found by the best fit to various β values in Table 1 with respect to different electric fields and can be interpreted as a weak field-dependence in the volume recombination.

2.2.2 Parameters determination for ERs

Similarly for ERs, one can use the LUX tritium data [27] to determine t_{pa} , α and β for ERs using Eq. 9 and Eq. 10 at which L is Lindhard quenching (Eq. 11), $W_i = 15.6$ eV, and $\frac{N_{ex}}{N_i} = 0.1387$. Figure 5 shows the best fit to the LUX tritium data obtained with an electric field of 180 V/cm.

As stated above, the external field cannot penetrate the ionization zone, t_{pa} is independent of electric field for ERs as well. The power-law field dependence of α and β is determined with two data sets taken from the LUX tritium calibration at 105 V/cm and 180 V/cm as well as one data set at 3750 V/cm taken by D. Yu. Akimov et al. in 2014. Figure 6 shows a weak dependence on electric field for data taken under relatively comparable electric fields. If the

Table 1

The obtained values of β in t_{pl} for NRs with respect to different fields with a fixed $\alpha = 3.617 \pm 0.521$ ns.

F (V/cm)	β (ns)	χ^2/ndf
100	1.409 ± 0.199	9.335/8
181	1.313 ± 0.196	4.299/9
270	1.243 ± 0.223	1.408/9
530	1.153 ± 0.148	3.274/4
730	1.129 ± 0.132	32.25/22
1000	1.096 ± 0.159	7.149/8
2030	1.025 ± 0.120	4.951/9
4000	0.962 ± 0.107	1.269/3

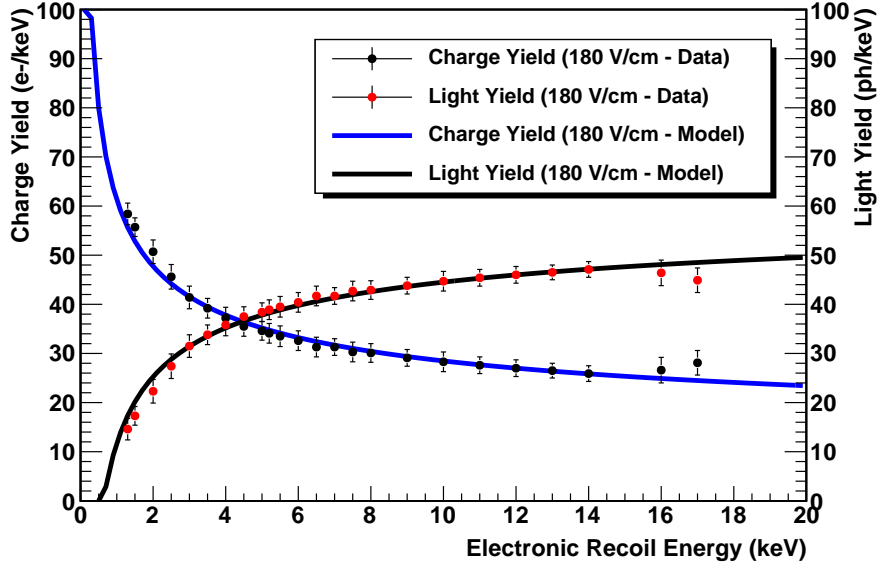


Fig. 5. Determination of t_{pa} , α and β by fitting Eq. 9 and Eq. 10 into the LUX tritium data with 180 V/cm [27]. The model predicts that $t_{pa} = 1.5 \pm 0.3$ ns, $\alpha = 7.425 \pm 0.147$ ns and $\beta = -0.198 \pm 0.069$ ns at 180 V/cm with $\chi^2/ndf = 12.97/23$. The word “Model” in the legend represents the generic model with the Wang-Mei’s recombination probability from this work.

electric field varies dramatically, the model defined by the parameters obtained under low electric fields (105 V/cm and 180 V/cm) cannot fit well with data taken under a very high electric field (3750 V/cm).

Once again, the field dependent values of δ_1 and δ_2 in Eq.7 and Eq. 8 for ERs

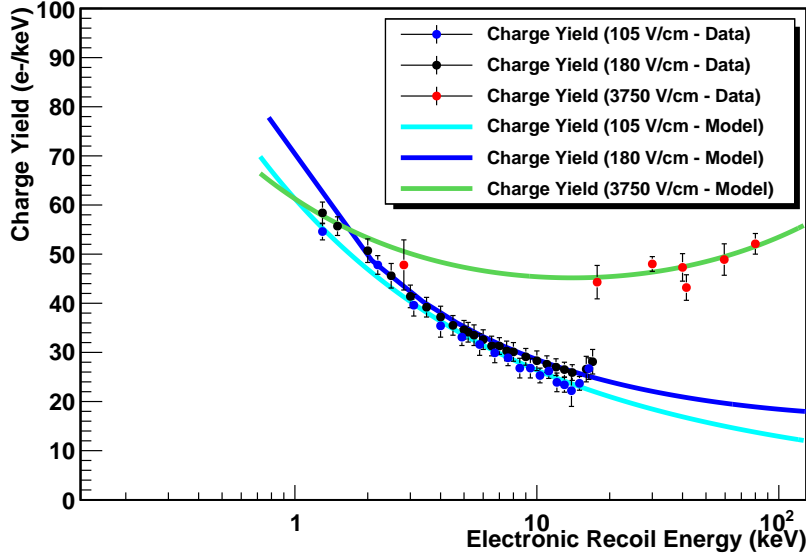


Fig. 6. A charge yield comparison between the generic model in Eq. 9 and data taken with different field strengths using the plasma time determined from the LUX tritium data. The data is taken from the LUX tritium calibration obtained with 105 V/cm, 180 V/cm, and D. Yu. Akimov et al. (2014) [28]. The word “Model” in the legend represents the generic model with the Wang-Mei’s recombination probability from this work.

Table 2

The obtained values of α and β for ERs with respect to different fields.

F (V/cm)	α (ns)	β (ns)	χ^2/ndf
105	8.073 ± 0.819	-0.176 ± 0.071	8.467/15
180	7.425 ± 0.147	-0.198 ± 0.069	12.97/23
3750	4.678 ± 0.927	-0.899 ± 0.240	4.414/5

are found by the best fit to various α and β values in Table 2 with respect to the three electric fields, and can be interpreted as a stronger field dependence in the volume recombination. Figure 7 shows the field dependence of the plasma time for ERs. t_{pl} is much larger at a lower electric field, which indicates more electrons recombine with ions in the volume recombination zone in contrast to that under a higher electric field.

Figure 8 shows the plasma time as a function of recoil energy for two types of events under the same electric field. The plasma time for NRs is much larger than that for ERs at a field of 4000 V/cm. This is because the plasma effect depends largely on the ionization density. The higher density of ionization track for NRs induces a stronger internal electric field that shields the influence of external electric field so that the plasma zone can retain thermal electrons

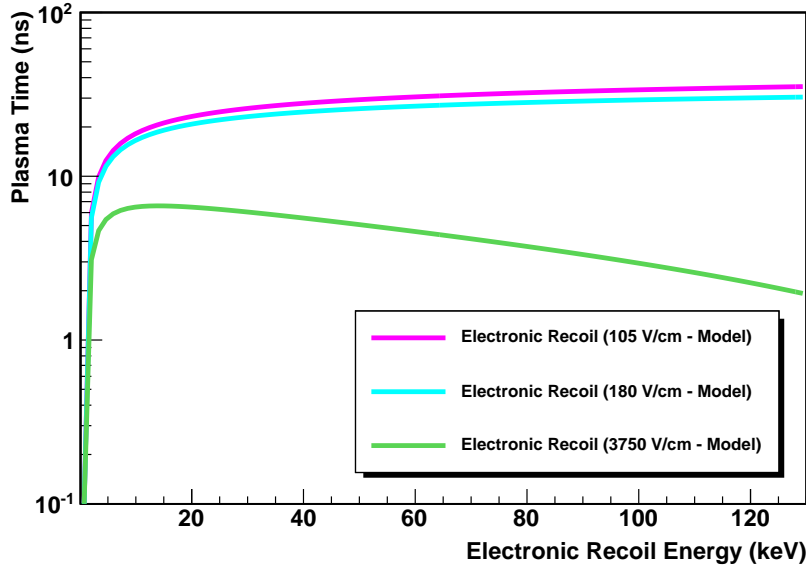


Fig. 7. Shown is the plasma time, t_{pl} , for ERs under different electric fields. The word “Model” in the legend represents the generic model with the Wang-Mei’s recombination probability from this work.

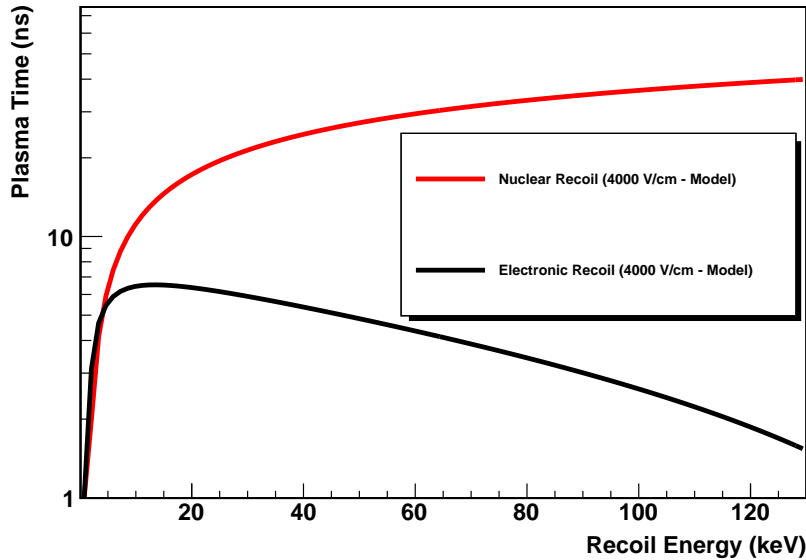


Fig. 8. Shown is the plasma time, t_{pl} , as a function of recoil energy under an electric field of 4000 V/cm. The word “Model” in the legend represents the generic model with the Wang-Mei’s recombination probability from this work.

for a longer plasma time, which results in more electrons recombining with ions in a higher density plasma volume.

Combining the plasma time with the effect of the parent recombination time, Figure 9 shows the recombination probability as a function of recoil energy at

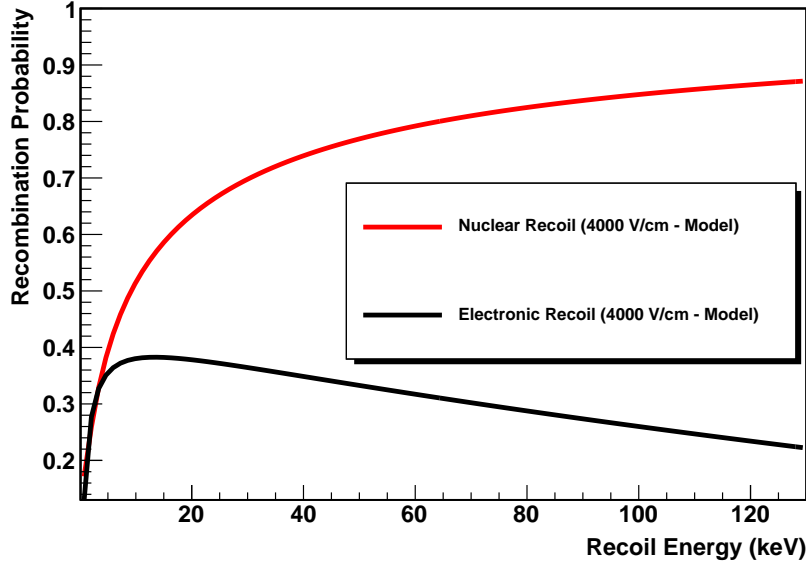


Fig. 9. Shown is the recombination probability as a function of recoil energy at a non-zero field with $F = 4000 \text{ V/cm}$. The word “Model” in the legend represents the generic model with the Wang-Mei’s recombination probability from this work.

4000 V/cm, more electrons will recombine with ions for NRs than ERs at a given energy.

We summarize the values of the parameters from Eq. 7 and Eq. 8 for NRs in Table 3, and for ERs in Table 4. The uncertainty of these parameters for ERs is as large as $\sim 10\%$ due to the insufficient data at different fields for the best fit. Therefore, more data taken under different fields would improve the accuracy of these parameters.

Table 3

The obtained parameters for NRs in Eq. 7 and Eq. 8 with a $\chi^2/\text{ndf} = 0.4407/6$.

α	3.617 ± 0.521
ns	
γ_2	2.102 ± 0.876
ns	
δ_2	-0.0943 ± 0.0678

2.3 Volume recombination time for zero field

Without an external electric field, the volume recombination time t_v depends on the initial number of e-ion pairs and ambipolar diffusion, and is expected

Table 4

The obtained parameters for ERs in Eq. 7 and Eq. 8. The value of χ^2/ndf for obtaining γ_1 and δ_1 is 0.0002307/1 and the value of χ^2/ndf for obtaining γ_2 and δ_2 is 0.06632/1.

γ_1	16.39±5.31
ns	
δ_1	-0.1525±0.0622
γ_2	-0.01735±0.01393
ns	
δ_2	0.4791±0.118

to be energy dependent with the same parametrization function as Eq. 6. The free parameters α and β are obtained by normalizing the scintillation efficiency from the generic model (Eq.10) to the available data for ERs [16,75], and NRs [25,29,30,31,32,33,34]. The functions describing the volume recombination time are found to be:

ERs:

$$t_v^{er} = (4.15 \pm 0.12) \times 10^3 \times (\ln E_{er}) + (3.444 \pm 0.101) \times (\ln E_{er})^2, \quad (14)$$

where the fitted $\chi^2/\text{ndf} = 1.234/4$.

NRs:

$$t_v^{nr} = (14.712 \pm 1.14) \times (\ln E_{nr}) + (2.444 \pm 0.132) \times (\ln E_{nr})^2, \quad (15)$$

where the fitted $\chi^2/\text{ndf} = 1.726/5$.

As shown in Figure 10, t_v of NRs is much smaller than that of ERs. This is because the ionization density of ERs is relatively smaller than that of NRs. A smaller ionization density for ERs generates a weaker internal electric field, allowing the electrons to diffuse farther away from the ionization track as illustrated in Figure 11. Without an electric field, these electrons can undergo multiple scattering before recombining with ions.

Figure 10 shows the values of t_v for ERs have a good agreement with [50]. At zero field, for both NRs and ERs, $t_v > t_{pa}$: more electrons recombine with ions within the volume recombination zone. As a result, shown in Figure 12, the recombination probability for ERs is 1; for NRs, it is slightly dependent on recoil energy in the region below 30 keV. This is because the ionization tracks for NRs with energy below 30 keV is shorter than Debye length [76] and cannot form any significant plasma effect. Therefore, the electrons are

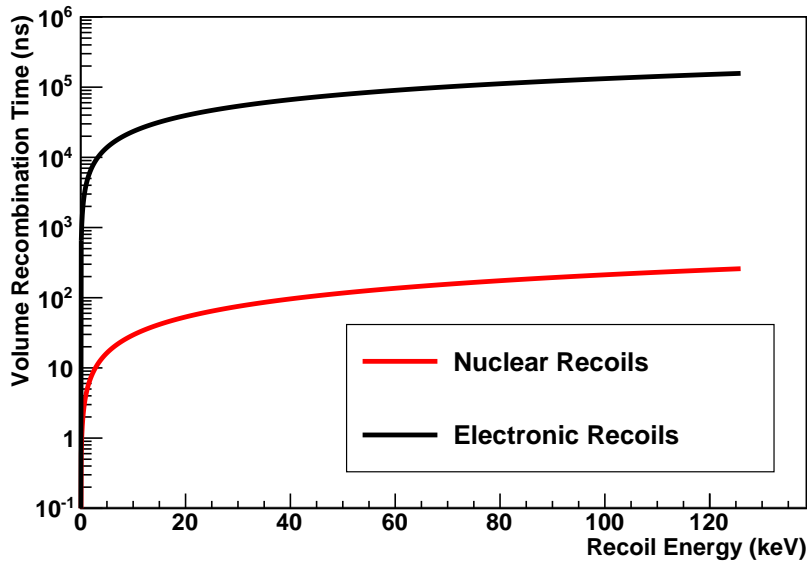


Fig. 10. Shown is the volume recombination time at zero field as a function of recoil energy. The curves are obtained using the generic model with the Wang-Mei's recombination probability from this work.

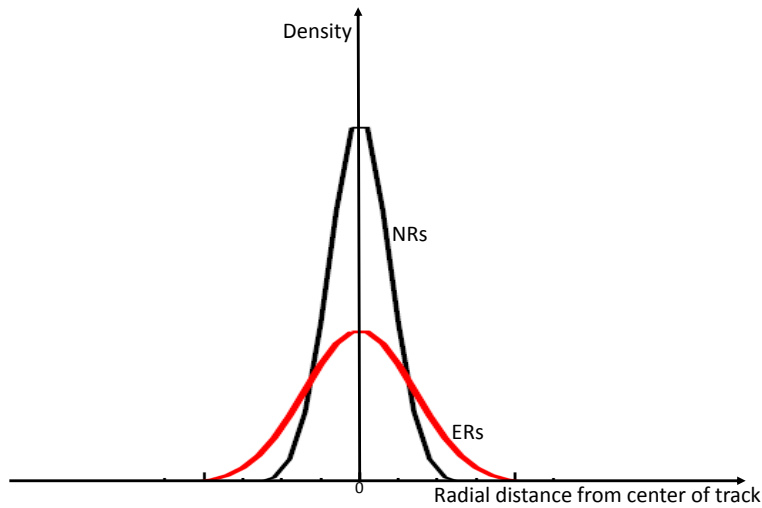


Fig. 11. Shown is a sketch of the density of plasma tracks versus the distance from center of the plasma tracks for ERs and NRs.

diffused away from the ionization track. Hence, the recombination probability decreases as the recoil energy decreases.

Utilizing the recombination model in this work, one can calculate the recombination probability at any given field and zero field for a liquid xenon detector. This recombination model is valid over the energy range of 0.1 – 130 keV.

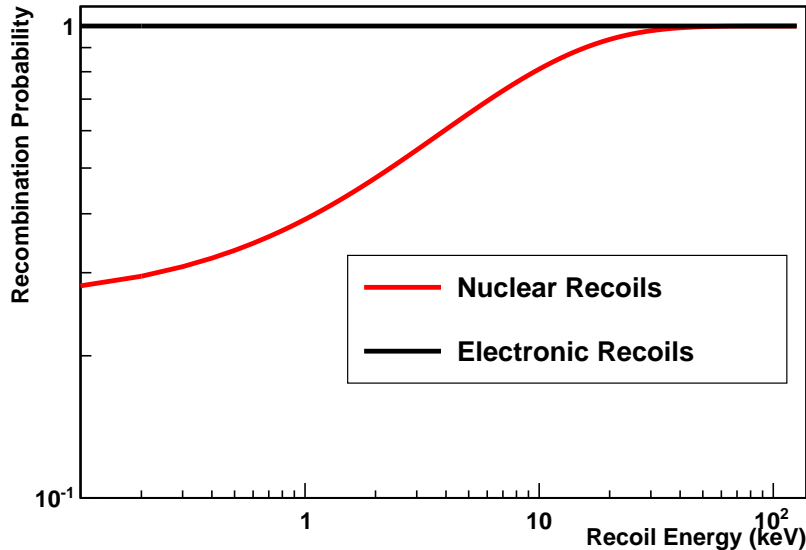


Fig. 12. Shown is the recombination probability as a function of recoil energy at zero field. The curves are obtained using the generic model with the Wang-Mei’s recombination probability from this work.

3 Implementation of the Model

3.1 Non-zero field

At non-zero fields, the plasma time can be calculated with Eq. 6, using the given values of α , γ , and δ in Table 3 and Table 4; the recombination probability is then obtained from Eq. 5 for a given energy in the energy range of 0.1 – 130 keV. The W_i -value is also energy dependent. Though the variation is small, its energy dependence could cause an uncertainty of 5% in energy reconstruction for recoil energy below 5 keV. Additionally, the Lindhard quenching factor is applied to the calculation of charge and light yield. The calculated charge yield from Eq. 9 in units of e^-/keV for NRs and ERs are compared with available data in Figure 13, Figure 14, and Figure 15, respectively. It is shown that the charge yield of ERs from this work (the model) agrees well with the data sets used in Figure 14. In Figure 15, our model agrees with the data from D. Yu. Akimov et al. (2014) [28] and partly agree with the work from Qing Lin et al. (2015) [77] based on the Thomas-Imel box model with the updated $4\xi/N_i$.

Clearly, for NRs, the model is weakly field dependent, and fits existing data very well. As discussed in Section 2.3.2, the plasma time for NRs increases from a few nanoseconds to a few tens of nanoseconds. Hence, the charge yield shown in Figure 13 is energy dependent in the energy range of interest.

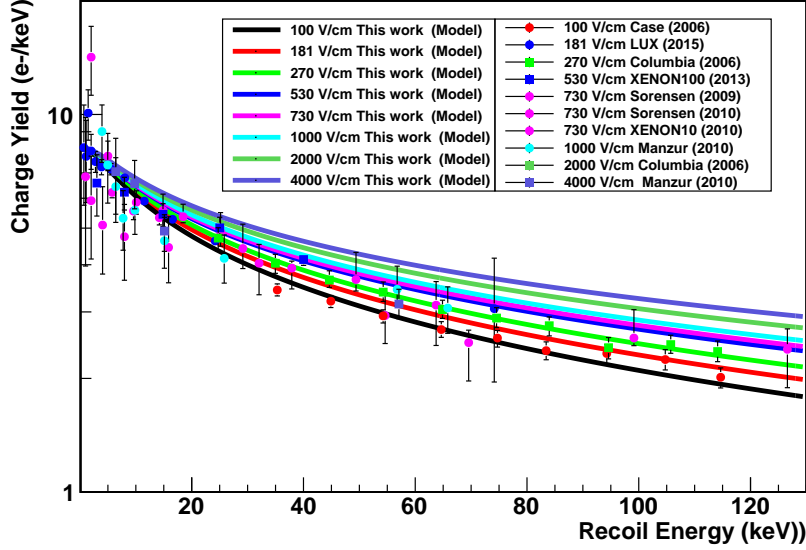


Fig. 13. All measurements of the charge yield of NRs in comparison with the generic model in Eq. 9 at different fields. The data in this plot are from Case (2006) at 100 V/cm [14], LUX D-D (2015) at 181 V/cm [19], Columbia (2006) at 270 V/cm [14], XENON100 (2013) at 530 V/cm [21], Sorensen (2009) at 730 V/cm [22], Sorensen (2010) at 730 V/cm [23], XENON10 (2010) at 730 V/cm [24], Manzur (2010) at 1000 V/cm [25], Columbia (2006) at 2000 V/cm [14], and Manzur (2010) at 4000 V/cm [25]. The word “Model” in the legend represents the generic model with the Wang-Mei’s recombination probability from this work.

However, for ERs, it is seen in Figure 7, the plasma time strongly depends on the applied field. At a lower field, the plasma time ranges from a few nanoseconds to a few tens of nanoseconds. However, the plasma time varies in a narrow range across the entire energy at a higher electric field (~ 4000 V/cm), the total recombination probability is also small as shown in Figure 9. Therefore, the charge yield (e^-/keV) of ERs under a higher field is very weakly dependent on the recoil energy, shown in Figure 14. Whereas the volume recombination probability under low fields (\sim a few hundreds V/cm) is much larger, due to the large plasma time that increases from a few nanoseconds to a few tens of nanoseconds as shown in Figure 7. Thus, the charge yield (e^-/keV) of ERs under a lower field is strongly dependent on the recoil energy.

3.2 Zero field

At zero field, the volume recombination time is calculated from Eq. 14 (Eq. 15) for ERs (NRs), and then the recombination probability is found from Eq. 5. The variation of the W_i -value, Eq.12, is applied. Both the Lindhard quenching factor (Eq.11) and the Hitachi quenching factor, 0.68 [36], are applied in the

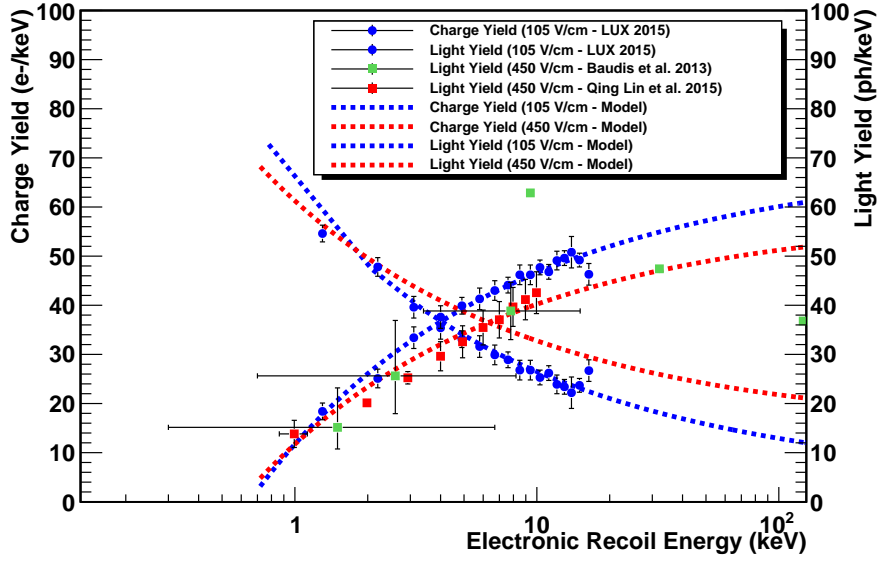


Fig. 14. The charge yield of ERs in comparison with the generic model in Eq. 9. The data is taken from the LUX tritium calibration obtained with 105 V/cm, Qing Lin et al. (2015) [77], and Baudis et al. (2013). The word “Model” in the legend represents the generic model with the Wang-Mei’s recombination probability from this work.

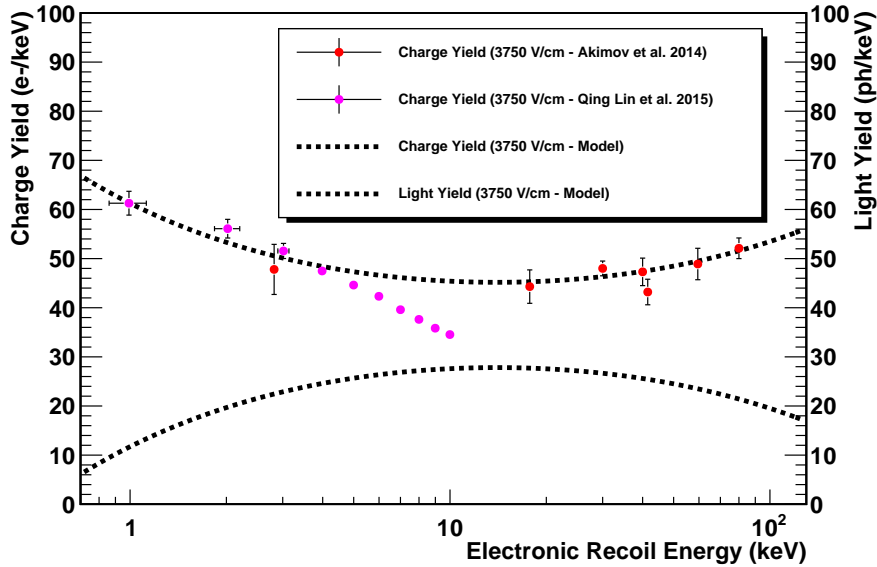


Fig. 15. The charge yield of ERs in comparison with the generic model in Eq. 9. The data is taken from D. Yu. Akimov et al. (2014) [28] and Qing Lin et al.(2015) [77]. The word “Model” in the legend represents the generic model with the Wang-Mei’s recombination probability from this work.

light yield for NRs. The quenching factor q_e (Eq. 16), from the best-fit to the data [75] as shown in Figure 16, is applied to ERs. The fitted function with a

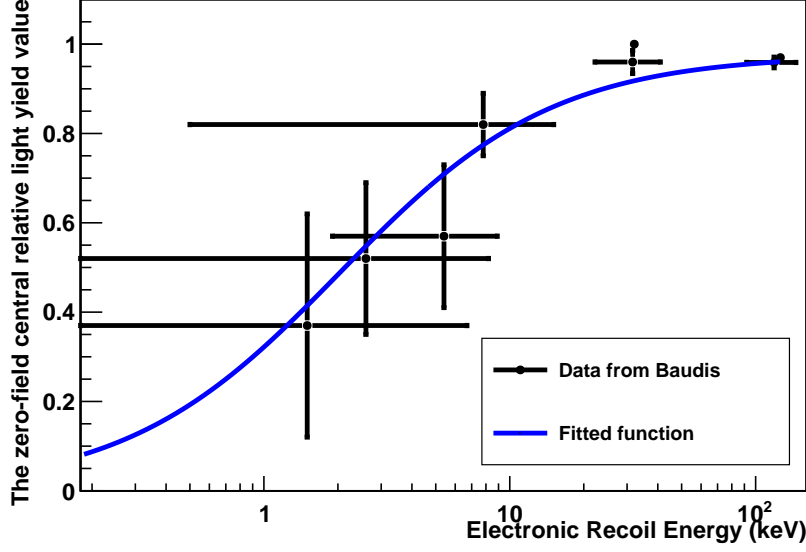


Fig. 16. The zero-field central relative light yield value (relative to the scintillation emission at 32.1 keV) as a function of electronic recoil energy. The data points are from Baudis et al. [75].

$\chi^2/\text{ndf} = 3.55/3$ following the form of Birks' law can be expressed as:

$$q_e = \frac{0.982 \pm 0.018 E_{er}}{1.999 \pm 0.003 + 0.96 \pm 0.02 E_{er}}. \quad (16)$$

Thus, the quenching factor, $L = q_e$, in Eq. 3 for ERs. Note that this is different to the explanation of the reduction of the light yield using the existence of the effect of escaping electrons in the absence of an electric field [72]. The resulting light yield at zero field for ERs and NRs, shown in Figure 17, indicates there exists a light reduction for ERs and NRs at very low energies.

To compare the generic model (Eq.10) with published data, we normalize the calculated scintillation efficiency to an absolute light yield of $L_y^{er} = 67$ photons/keV at 122 keV from ^{57}Co . Figure 18 shows a good agreement between the calculation of Eq. 3 and the published measurements. Hence, the generic model of the W_i -value, the quenching factors, and recombination proposed in this work combine to produce valid results.

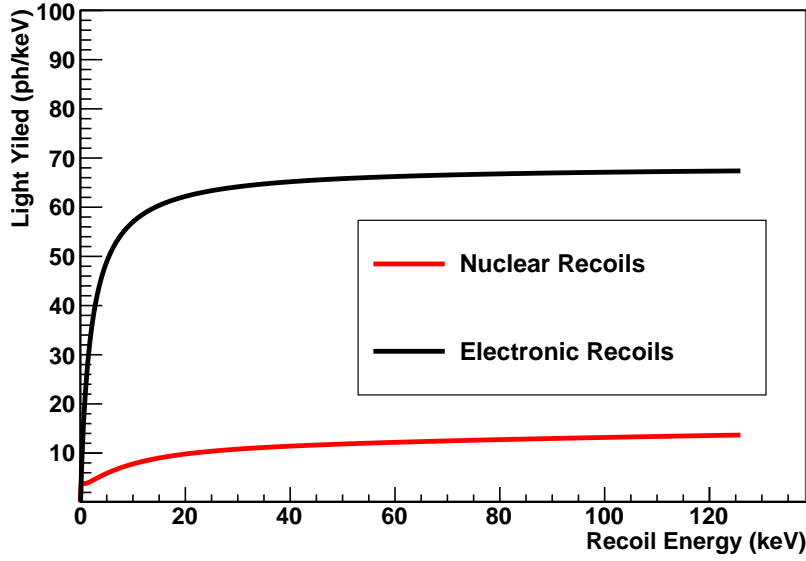


Fig. 17. Light yield calculated from the generic model in Eq. 3 at zero field with the Wang-Mei's recombination probability from this work.

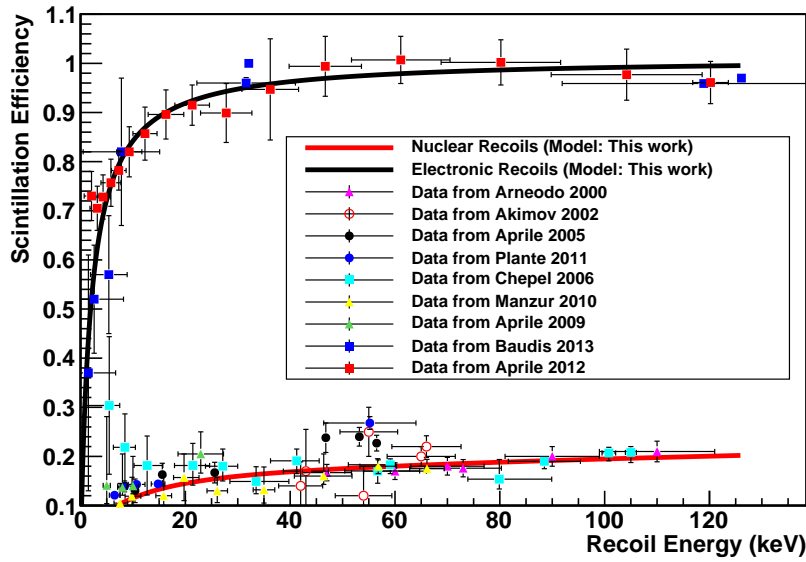


Fig. 18. All measurements of the scintillation efficiency ($\frac{n_\gamma}{L_{er}^{er} \times E_0}$) in comparison with the generic model expressed by Eq. 3 at zero field. The data in this plot are from Arneodo 2000 [29], Akimov 2002 [30], Aprile 2005 [31], Plante 2011 [32], Chepel 2006 [33], Manzur 2010 [25], Aprile 2009 [34]. The word “Model” in the legend represents the generic model with the Wang-Mei's recombination probability from this work.

4 Summary and remarks

4.1 Non-zero field

We summarize the parameters used in Eq. 9 and Eq. 10 to calculate the charge and light yield for NRs and ERs in Table 5. Note that the parameters in Eq. 8 Table 5

The summary of the parameters used in Eq. 9 and Eq. 10.

	L	W_i	t_c	t_{pa}	α	β	$\frac{N_{ex}}{N_i}$
NRs	Eq. 11	Eq. 12	15 ns	1.5 ns	3.617 ± 0.521 ns	Eq. 8	Eq. 13
ERs	1.0	15.6 eV	15 ns	1.5 ns	Eq. 7	Eq. 8	0.1387

for NRs are listed in Table 3. Similarly, the parameters in Eq. 7 and Eq. 8 are summarized in Table 4. The parameters used in Eq. 11 and Eq. 12 are described in subsection 2.2.1.

As we have shown in Section 3, in addition to the Lindhard quenching factor, the charge and light yield under an electric field is mainly driven by the recombination probability. The parent recombination probability is about 6.7% for NRs and ERs determined by the parent recombination time of 1.5 ns. On the one hand, It is seen that the plasma time plays an important role in the recombination for NRs as shown in Figure 19, which illustrates that the charge yield is inversely proportional to the plasma time. On the other hand, the plasma time for ERs changes with different electric fields as shown in Figure 7 in Section 2.3.2. This indicates that the recombination probability for ERs slightly decreases at high electric fields. While at low electric fields, the plasma time varies as a function of recoil energy. Hence the the recombination probability depends strongly on recoil energy.

As demonstrated by LUX, XENON100, and XENON10 [9,10,17], the ratio of S2 to S1 can be used to discriminate NRs and ERs, as predicted by both our model and NEST as shown in Figure 20. One can also use $\text{Log}_{10}(S2)$ versus $S1$ to discriminate NRs from ERs as illustrated in Figure 21 with an electric field of 180 V/cm. The limitation of the separation between NRs and ERs would be only constrained by the energy resolution [78] in the region of interest. Note that the prediction from our model and NEST, as shown in Figure 21, agrees with the recent LUX analysis that has improved the sensitivity of the WIMP searches [19].

Since the difference of the plasma time between NRs and ERs is up to 10–50 ns at a high electric field (4000 V/cm), shown in Figure 8, this would imply a large difference in charge and light yield between ERs and NRs. As a result, the charge yield from ERs at a high field (4000 V/cm) is a constant at a level

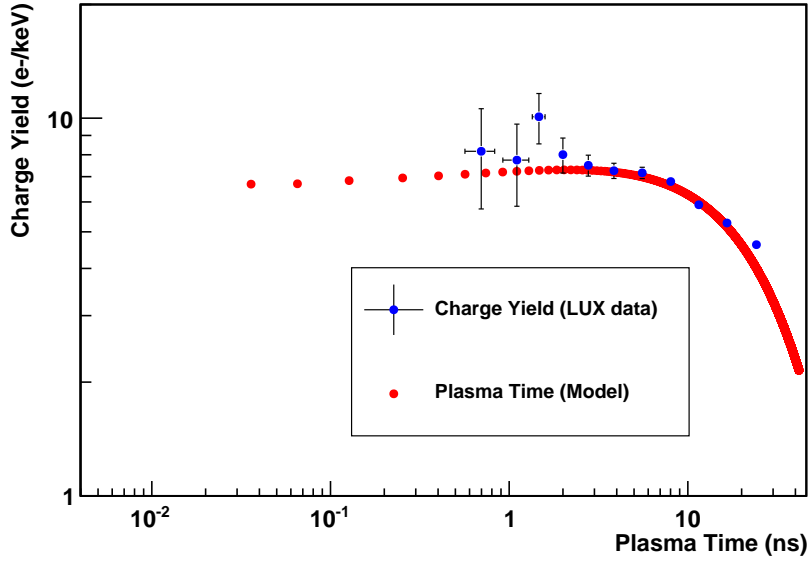


Fig. 19. Shown is the correlation between charge yield and plasma time for NRs in comparison with LUX D-D data [19]. The blue dots are from the LUX D-D data and the red dots are calculated plasma time using Eq. 6.

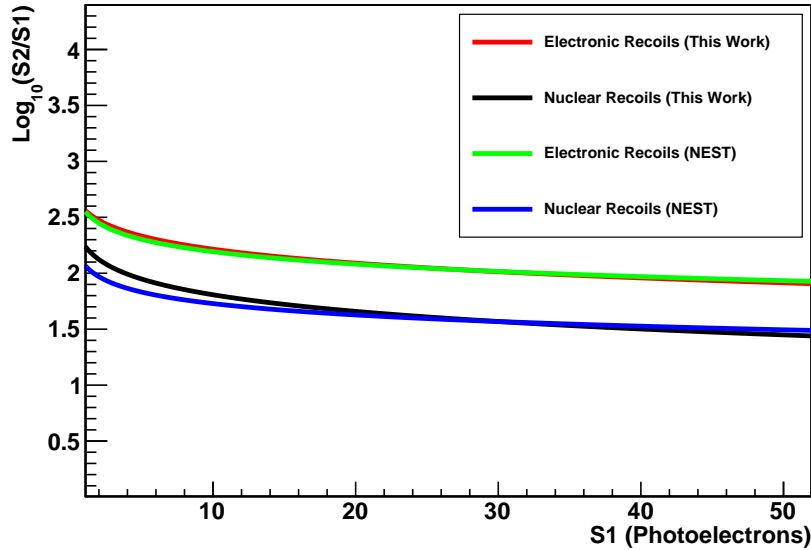


Fig. 20. Shown is the predicted separation between NRs and ERs using the ratio of S2 to S1. The gain factors $g_1 = 0.14$ and $g_2 = 24.55$, from LUX [9], are used with a field of 180 V/cm to generate the plot. Note that the parameters used in the NEST model are the best-fit parameters obtained with the LUX DD neutron data and the LUX tritium data.

of $\sim 50 e^-/keV$ while the charge yield from NRs varies as a function of recoil energy, at a level of less than $10 e^-/keV$. Such a large difference could enhance the separation between NRs and ERs. In theory, the minimum external field

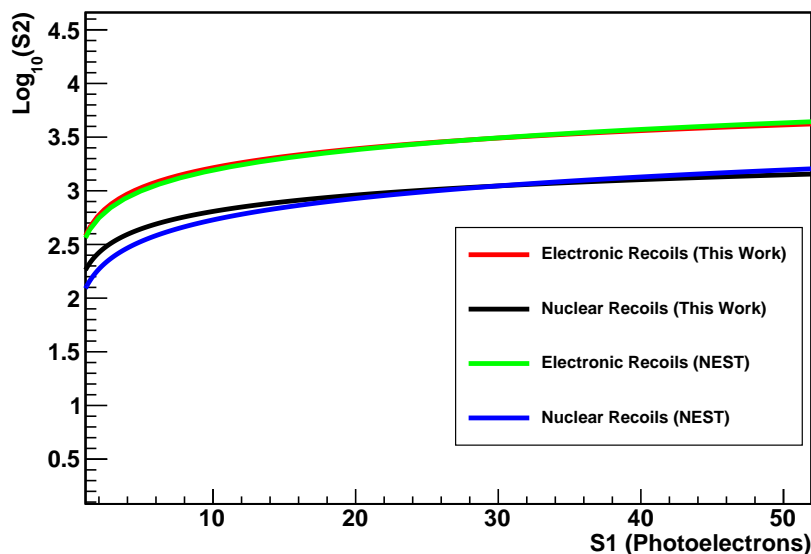


Fig. 21. Shown is the predicted separation between NRs and ERs using $\text{Log}_{10}(S2)$ versus $S1$ analysis. The gain factors $g_1 = 0.14$ and $g_2 = 24.55$, from LUX [9], are used with a field of 180 V/cm to generate the plot. Note that the parameters used in the NEST model are the best-fit parameters obtained with the LUX DD neutron data and the LUX tritium data.

required to drift electrons away is $F = \frac{v_s}{\mu}$, where v_s is the speed of sound and μ is electron mobility. For liquid xenon, $F \geq 34.2$ V/cm.

4.2 Zero field

We summarize the parameters used in Eq. 10 to calculate the light yield for NRs and ERs in Table 6. Note that the parameters used in Eq. 11 and Eq. 12

Table 6

The summary of the parameters used in Eq. 10.

	L	W_i	t_c	t_{pa}	α	β	$\frac{N_{er}}{N_i}$
NRs	Eq. 11 $\times 0.68$	Eq. 12	15 ns	1.5 ns	14.712 ± 1.14 ns	2.444 ± 0.132	Eq. 13
ERs	Eq. 16	15.6 eV	15 ns	1.5 ns	$(4.15 \pm 0.12) \times 10^3$	3.444 ± 0.101	0.1387

are described in subsection 2.2.1 and the parameters used in Eq. 16 are defined in subsection 3.2.

In the case of zero field, the light yield for NRs is governed by both recombination and quenching factors. As can be seen in Figure 12, the recombination probability decreases as recoil energy decreases in the energy region below 30 keV for NRs, and electrons escape recombination with xenon ions. These

escaping electrons may be neutralised by hitting non-xenon detector components, which will not contribute to the light yield in xenon. When the nuclear recoil energy is greater than 30 keV, the recombination probability becomes 1. The reduction of scintillation efficiency is then solely governed by the quenching factor. For ERs, the recombination probability is 1 across the entire recoil energy of interest due to the volume recombination time being greater than 10 μ s. The reduction of scintillation efficiency is solely due to the scintillation quenching. It is worth mentioning that the e-ion pairs produced by NRs take a shorter time to recombine (less than 200 ns) while e-ion pairs generated by ERs take a much longer time to recombine (greater than 10 μ s).

5 Conclusions

We report a coherent and comprehensive model of light and charge yield by calculating the average energy expended per e-ion pair, the quenching factors, and the recombination probability in liquid xenon for both non-zero field and zero field. As a result, we show that the calculations of n_γ and n_e using the energy-dependent W_i -value, quenching factors, and the field-dependent recombination probability agree with the available experimental results. A recombination model developed in this work explains the recombination process in liquid xenon, and predicts the dependence on recoil type, electric field, and recoil energy in the recombination probability. At non-zero field, the charge and light yield for NRs are dominated by both recombination and Lindhard quenching factor. While the charge and light yield for ERs are governed by recombination only. At zero field, the light yield for NRs is affected by the quenching factors through Lindhard and Hitachi mechanisms. In the case of ERs, the e-ion recombination is 100% and the light yield is reduced by the scintillation quenching following Birks' law. We find that the plasma time is a main factor that governs the charge and light yield to discriminate NRs from ERs.

Acknowledgments

The authors wish to thank Christina Keller and Amy Roberts for their careful reading of this manuscript. Additionally, the authors would like to thank Dan McKinsey for his comments and suggestions. This work was supported in part by NSF PHY-0919278, NSF PHY-1242640, DOE grant DE-FG02-10ER46709, the Office of Research at the University of South Dakota and a research center supported by the State of South Dakota.

References

- [1] F. Zwicky, Die Rotreschiebung von extragalaktish Nebeln, *Helv. Phys. Acta* 6 (1933) 110-127.
- [2] G. Hinshaw et al. (WMAP Collaboration), <http://arxiv.org/abs/1212.5226v3>.
- [3] R. J. Gaitskell, *Ann. Rev. Nucl. Part. Sci.* 54 (2004) 315-359.
- [4] J. L. Feng, *Annals of Physics* 315, Issue 1 (2005) 2-15, <http://arxiv.org/abs/hep-ph/0405215>.
- [5] M. W. Goodman and E. Witten, *Phys. Rev. D* 31 (June, 1985) 3059-3063.
- [6] M. Turner, Committee on the Physics of the Universe, National Research Council, Washington, D.C., The National Academies Press, 2003.
- [7] Particle Physics Project Prioritization Panel (P5), "US Particle Physics: Science Opportunities: A Stratetic Plan for the Next Ten Years."
- [8] D. S. Akerib et al. (LUX Collaboration), *Nucl. Instrum. Meth. A* 704, 111-126 (2013) <http://arxiv.org/abs/1211.3788>.
- [9] D. S. Akerib et al. (LUX Collaboration), *Phys. Rev. Lett.* 112, 091303 (2014).
- [10] E. Aprile et al. (XENON100 Collaboration), *Phys. Rev. Lett.* 109, 181301 (2012).
- [11] Mengjiao Xiao et al. (PandaX Collaboration), *Sci.China Phys. Mech. Astron.* 57 (2014) 2024-2030.
- [12] D. S. Akerib et al. (LZ Collaboration), [arXiv:1509.02910](https://arxiv.org/abs/1509.02910).
- [13] E. Aprile et al. (XENON1T Collaboration), [arXiv:1503.07698](https://arxiv.org/abs/1503.07698).
- [14] E. Aprile et al., *Phys. Rev. Lett.*, vol. 97, p. 081302, Aug 2006.
- [15] E. Aprile, K. L. Giboni, P. Majewski, K. Ni, and M. Yamashita, *Phys. Rev. B*, vol. 76, p. 014115, Jul 2007.
- [16] E. Aprile and T. Doke, *Rev. Mod. Phys.* V82 (2010) 2053.
- [17] J. Angle et al. (XENON10 Collaboration), *Phys. Rev. Lett.* 101, (2008) 091301.
- [18] R. L. Platzman, 1961, *J. AppLRadiat. Isot.* 10, 116-127.
- [19] D. S. Akerib et al. (LUX Collaboration), *Phys. Rev. Lett.* 116, 161301 (2016), [arXiv:1512.03506v2](https://arxiv.org/abs/1512.03506v2).
- [20] J. Lindhard, et al., *Mat. Fis. Medd. Dan. Vidensk. Selsk.* 33 (10) (1963).
- [21] E. Aprile et al., *Phys. Rev. D*, vol. 88, p. 012006, Jul 2013.
- [22] P. Sorensen et al., *Nucl. Instr. and Meth. in Phys. Res. A*, vol. 601, no. 3, pp. 339-346, 2009.

- [23] P. Sorensen, *Journal of Cosmology and Astroparticle Physics*, vol. 2010, no. 09, p. 033, 2010.
- [24] P. Sorensen et al., *PoS*, vol. IDM2010, p. 017, 2011.
- [25] A. Manzur, A. Curioni, L. Kastens, D. N. McKinsey, K. Ni, and T. Wongjirad, *Phys. Rev. C*, vol. 81, p. 025808, Feb 2010.
- [26] T. Takahashi et al., *Phys. Rev. A*, V 12, (1975) 1771.
- [27] D. S. Akerib et al., *Phys. Rev. D* 93, 072009 (2016), arXiv:1512.03133v1.
- [28] D. Yu. Akimov et al., *JINST* 9 (2014) no.11, P11014.
- [29] F. Arneodo et al., *Nucl. Instr. and Meth. in Phys. Res. A*, vol. 449, no. 1-2, pp. 147-157, 2000.
- [30] D. Akimov et al., *Physics Letters B*, vol. 524, no. 34, pp. 245-251, 2002.
- [31] E. Aprile et al., *Phys. Rev. D*, vol. 72, p. 072006, Oct 2005.
- [32] G. Plante et al., *Phys. Rev. C*, vol. 84, p. 045805, Oct 2011.
- [33] V. Chepel et al., *Astropart. Phys.* 26 (2006) 5863.
- [34] E. Aprile et al., *Phys. Rev. C*, vol. 79, p. 045807, Apr 2009.
- [35] T. Doke, A. Hitachi, J. Kikuchi, K. Masuda, H. Okada, and E. Shibamura, *Japanese Journal of Applied Physics*, vol. 41, no. 3R, p. 1538, 2002.
- [36] A. Hitach, *Astropart. Phys.* 24, 247 (2005).
- [37] D.-M. Mei, Z.-B. Yin, L. C. Stonehill, A. Hime, *Astropart. Phys.* 30 (2008) 12-17.
- [38] P. Sorensen et al., *Nucl. Instr. and Meth. in Phys. Res. A*, vol. 601, no. 3, pp. 339 346, 2009.
- [39] P. Sorensen and C. E. Dahl, *Physical Review D*, vol. 83, no. 6, p. 063501, Mar. 2011.
- [40] F. Bezrukov, F. Kahlhoefer, and M. Lindner, *Astroparticle Physics*, vol. 35, no. 3, pp. 119 127, 2011.
- [41] M. Szydagis et al., *JINST*, vol. 6, p. P10002, 2011.
- [42] M. Szydagis, A. Fyhrie, D. Thorngren, and M. Tripathi, *JINST*, vol. 8, p. C10003, 2013.
- [43] E. Aprile et al., *Phys. Rev. D*, vol. 88, p. 012006, Jul 2013.
- [44] J. Mock et al., *JINST*, vol. 9, p. T04002, 2014.
- [45] M. Foxe et al., *Nucl. Inst. and Methods in Phys. Res. A*, vol. 771, pp. 88 92, 2015.
- [46] W. Mu and X. Ji, *Astroparticle Physics*, vol. 62, pp. 108 114, 2015.

- [47] W. Mu, X. Xiong, and X. Ji, *Astroparticle Physics*, vol. 61, pp. 56–61, 2015.
- [48] Brian Lenardo et al., *IEEE Trans. on Nucl. Sci.* 62 (2015) 3387. arXiv:1412.4417v2, 16 Dec 2014.
- [49] Shinzou Kubota et al., *Phys. Rev. B* V20 3486 (1979).
- [50] B. A. Dolgoshein, V. N. Lebedenko, A. M. Rogozhin, B. U. Rodionov and E. N. Shuvalova, *Zh. Eksp. Teor. Fiz.* 56, 1152-1160 (April, 1969).
- [51] K. Ni, E. Aprile, K. L. Giboni, P. Majewski, and M. Yamashita, *J. Inst.* 1 (2006) P09004.
- [52] T. Doke et al., LET dependence of scintillation yields in liquid argon, *Nucl. Instrum. Meth.* A269 (1988) 291.
- [53] D. Dahl, The physics of background discrimination in liquid xenon, and the first results from Xenon10 in the hunt for WIMP dark matter, PhD thesis, Princeton University, 2009.
- [54] P. Sorensen and C. E. Dahl, *Phys. Rev.* D83 (2011) 063501.
- [55] J. Thomas and D. A. Imel, Recombination of electron-ion pairs in liquid argon and liquid xenon, *Phys. Rev.* A36 (1987) 614.
- [56] K. S. Song, *Can. J. Phys.* 49, 26 (1971).
- [57] S. D. Druger and R. S. Knox, *J. Chem. Phys.* 50, 3143 (1969).
- [58] P. G. LeComber, R. J. Loveland, and W. E. Spear, *Phys. Rev. B* 11, 3124 (1975).
- [59] M. Kizilyalli, J. Corish, R. Metselarr, *Pure Appl. Chem.* 71 (1999) 1307.
- [60] F. Bezrukov et al., *Astropart. Phys.*, 35 (2011), pp. 119-127, arXiv:1011.3990v2.
- [61] W. Seibt et al., *Nucl. Instrum. Methods*, v. 113, no. 3, pp. 317-324.
- [62] M. Szydagis et al., arXiv:1106.1613v1 (2011).
- [63] L. Onsager, *Phys. Rev.* v54, 15 Oct(1938).
- [64] S. Amoruso et.al. (ICARUS Collaboration) *Nucl. Instrum. Meth.* A523 (2004) 275-286.
- [65] D. R. Nygren, *Journal of Physics Conference Series* 460 (1): 2006, Sep 2013.
- [66] S. Basak and M.H. Cohen, *Phys. Rev. B* 20, 3404 (1979).
- [67] Ulrich Sowada et al., *Phys. Rev. B*, v. 25, n0. 5, 1982.
- [68] T. Steinberger et. al, in *Proceedings of the Second International Conference on Conduction in Low-Mobility Materials*, Eilat, Israel, 1971 (Taylor and Francis, London, 1971).
- [69] I. Roberts and E.G. Wilson, *J. Phys.* C6, 2169 (1973).

- [70] U. Asaf and I. T. Steinberger, Phys. Rev. B 10, 4464 (1974).
- [71] M. Miyajima et al., Phys. Rev. A9 (1974) 1438.
- [72] T. Doke et al., Jpn.J.Appl. Phys. 41, 1538 (2002).
- [73] Shankar Mukherji, Phys. Rev. B V12, (1975) 3530.
- [74] W. H. Barkas and M. J. Berger, Studies in Penetration of Charged Particles in Matter (National Academy of Sciences National Research Council, Washington, D.C. , 1964), Publication 1133, p. 103.
- [75] L. Baudis et al., Phys. Rev. D 87 (2013) 115017. arXiv:1303.6891v3.
- [76] P. C. Clemmow and J. P. Dougherty (1969). Electrodynamics of particles and plasmas. Redwood City CA: Addison-Wesley. pp. 7.6.7, p. 236 ff. ISBN 0-201-47986-9.
- [77] Qing Lin et al., Phys. Rev. D 92, 032005 (2015).
- [78] D.-M. Mei, W.-Z. Wei and L. Wang, arXiv:1512.00694v1.